Electronic supplementary information for

Hydrogen-bond regulation in organic/aqueous hybrid electrolyte for safe and high-voltage K-ion batteries

Maoting Xia,[a] Hongwei Fu,*[a] Kairui Lin,[b] Apparao M. Rao,[c] Limei Cha,[d] Huan Liu,[e] Jiang Zhou,[f] Chengxin Wang*[g] and Bingan Lu*[a]

[a] School of Physics and Electronics, Hunan University, Changsha, 410082, China.

[b] College of Design and Engineering, National University of Singapore, Singapore, 117575, Singapore.

[c] Department of Physics and Astronomy, Clemson Nanomaterials Institute, Clemson University, Clemson, SC 29634, USA.

[d] Materials Science and Engineering program, Guangdong Technion–Israel Institute of Technology, Shantou, 515063, China.

[e] College of Materials Science and Engineering, Hunan University of Science and Technology, Xiangtan, 411201, China.

[f] School of Materials Science and Engineering, Central South University, Changsha, 410083, China.

[g] School of Materials Science and Engineering, Sun Yat-sen University, Guangzhou, 510275, China.

*Corresponding author. E-mail: hongweifu@hnu.edu.cn (H. Fu); wchengx@mail.sysu.edu.cn (C. Wang); luba2012@hnu.edu.cn (B. Lu)

Experimental Methods

Materials. All chemicals were used as received. Succinonitrile (SCN, 99%), divanadium pentaoxide (V_2O_5, 98%), N,N-dimethylformamide (DMF, 99%), oxalic acid (99%), phosphorous acid (H_3PO_3, 99%), poly(vinylidene fluoride-co-hexafluoropropylene) (PVDF-HFP, Mw = 455,000) and dimethyl carbonate (DMC, 99%) were purchased from Sigma-Aldrich. Potassium bis(fluorosulfonyl)imide (KFSI, 99.9%) was purchased from Shanghai Songjing New Energy Technology Co., LTD. 3,4,9,10-perylenetetracarboxylic diimide (PTCDI, 95%) was purchased from TCI (Shanghai). N-Methyl-2-pyrrolidone (NMP, 99.5%) and potassium hydroxide (KOH, 95%) were purchased from Aladdin. Polyvinylidene fluoride (PVDF) and Super P were purchased from Shenzhen Kejing Star Technology. Deionized water for aqueous electrolytes was produced by a water purification system (Millipore, Milli-Q Intergral 15) and purged with Ar for 30 min before use to remove the dissolved oxygen.

Preparation of Electrolytes. Several eutectic KFSI/SCN mixtures with different molar ratios (1:1, 1:2, 1:4, 1:6, 1:8) were prepared via heating at 70°C for 4 h to form transparent solutions in order to determine the optimal eutectic ratio. Due to the high viscosity of KFSI/SCN eutectic solution, H_2O component was introduced in preparation to decrease the viscosity and increase the ionic conductivity of the electrolytes. The composition of the KFSI–SCN–H_2O hybrid electrolyte was shown in Table S1. In addition, contrast samples (5.6 m KFSI–H_2O and 30 m KFSI–H_2O aqueous electrolytes) were prepared by mixing stoichiometric KFSI with pure H_2O to obtain a clear liquid. All electrolytes were purged with Ar before use to remove the dissolved oxygen.

Preparation of KVPO$_4$F cathode material. V_2O_5 (20 mmol) and oxalic acid (60 mmol) were added to 30 mL H_2O and stirred vigorously at 70°C for 1 h, denoted as solution A. Meanwhile, KOH (120 mmol) and H_3PO_3 (120 mmol) were slowly added to 20 mL H_2O under stirring, denoted as solution B. After cooling to room temperature, solution B was added to solution A. The mixed solution was then transferred into a 100 mL Teflon-lined stainless-steel autoclave and maintained at 180°C for 12 h. The obtained light green precipitate was centrifuged, washed thoroughly, and dried in a vacuum oven at 80°C. Next, 5 wt% PVDF-HFP was dissolved in DMF at 50°C, and then the light green precursor was added under stirring to form a uniform slurry (the mass ratio of precursor and PVDF-HFP was 4:1). After the evaporation of DMF at 120°C with continuous stirring, the obtained solid product was annealed in a tube furnace at 650°C under Ar flow for 6 h to get the target product of KVPO$_4$F.

Electrode preparation and electrochemical measurements. The composite electrodes were prepared by mixing the active material (KVPO$_4$F or PTCDI), Super P, and PVDF in

NMP solvent at a mass ratio of 7:2:1. Then the obtained slurries were uniformly coated on the Ti mesh (200-mesh sieve) and dried at 100°C for 24 h. It has been reported in the literature that the response of Ti mesh to the decomposition of aqueous electrolyte is minimal, and the capacitance contribution is negligible.[1] Therefore, using Ti mesh as a current collector can accurately evaluate the electrochemical performance of the electrodes in this work. The electrochemical properties of $KVPO_4F$ cathode and PTCDI anode in the designed 5.6 m KFSI−SCN−H_2O electrolytes were tested in a three-electrode device with Pt and Ag/AgCl (0.222 V versus SHE) as counter and reference electrodes, respectively. For convenience, the potential versus Ag/AgCl reference was converted to K^+/K reference. $KVPO_4F$//PTCDI full cells were assembled in CR2032 coin cells with pre-cycled $KVPO_4F$ as the cathode, pre-cycled PTCDI as the anode, and glass fiber (Whatman, GF/D) as the separator. The diameter of the cathode and anode electrodes is 12 mm. The mass ratio of $KVPO_4F$/PTCDI was about 1.5/1. The electrolyte dosage for each coin cell was 150 µL. The capacity in full cells was calculated based on the total mass of cathode and anode materials. The energy density of full cell was calculated using the formula (Energy density = capacity × average voltage / total mass of cathode and anode). As for the pouch cells, the cathode electrode was cut into a size of about 6 × 6 cm, and the anode and separator were slightly larger than that. For the 5 mAh pouch cells, the mass loadings of $KVPO_4F$ and PTCDI were around 68 and 40 mg, respectively. The electrolyte dosage for each pouch cell was about 1.8 mL. All batteries were assembled in the air, and their electrochemical performance was evaluated on a battery testing system (LAND, CT2001A). Low-temperature electrochemical performance was evaluated on a battery testing system (LANHE, CT3002A) coupled with an environmental chamber (BTC-406) to control the testing temperature. The electrochemical stability windows of electrolytes were determined by linear sweep voltammetry (LSV) tests on an electrochemical workstation (CHI660e) using a three-electrode device with Ti mesh and Ag/AgCl as working and reference electrodes, respectively. The cyclic voltammetry (CV) curves were also recorded using the CHI660e electrochemical workstation at the scan rate of 1 mV s^{-1}. The in-situ electrochemical impedance spectroscopy (EIS) was conducted on a potential station (Admiral, SquidstatTM Prime Plus 1705) with a frequency ranging from 10^{-2} to 10^5 Hz.

Characterizations. The two-dimensional low-field nuclear magnetic resonance (2D LF–NMR, NMI20-030H-I, Shanghai Niumag Corporation, Shanghai, China) was used for the T_1–T_2 relaxation measurements to provide dynamics information for water molecules in electrolytes. The thermal stability of the eutectic electrolytes was conducted by differential scanning calorimeter (DSC) using a DSC 1 STAR^e System (METTLER TOLEDO). The samples were tested from −100°C to 20°C at a rate of 3°C min^{-1} under N_2 atmosphere. The physical and chemical properties of electrolytes were characterized by Raman spectra (Thermo Scientific DXRXI system) with a 532 nm excitation laser and attenuated total reflectance Fourier transform infrared spectrometry (ATR–FTIR, PerkinElmer Spectrum

II FT–IR Spectrometer). Raman and ATR–FTIR spectra of individual SCN and KFSI were used as references. tests. Viscosity of the electrolytes was measured on an Anton Paar MCR 302 rheometer at 30°C .The ionic conductivity of the electrolyte was measured on a conductivity meter (DDS-11A, INESA) at room temperature. The X-ray diffractometer (XRD) pattern of $KVPO_4F$ was recorded using a Bruker-AXS Micro-diffractometer (D8 ADVANCE) with Cu Kα radiation (λ = 1.5405 Å) at a scan range of 10°−80°. The CEI formed on the surface of cycled $KVPO_4F$ electrodes was characterized by transmission electron microscopy (TEM, Titan G2 60–300) and scanning transmission electron microscopy (STEM, Thermo Scientific Talos F200X) with elemental mappings analysis. The surface analysis of the cycled electrodes was performed by X-ray photoelectron spectroscopy (XPS, Thermo Fisher Scientific ESCALAB 250Xi System) and time-of-flight secondary ion mass spectrometry (ToF–SIMS, PHI nano TOF II). The scanning area of ToF-SIMS was 100×100 μm, and the sputtering speed was 0.1 nm s^{-1} for SiO_2. For the above interphase chemistry characterizations, the electrodes were cycled 20 times in electrolytes using three-electrode devices and then washed with DMC to remove the residual electrolytes.

MD simulations. Molecular dynamic (MD) simulations were carried out using the LAMMPS package.[2] The OPLS-AA force field[3] with fitted parameters for FSI- anions[4] and SCN molecules (from LigParGen)[5] were used in this work. H_2O molecules were simulated with TIP3P-FB model[6], and the parameters of K^+ cations fitted to TIP3P-FB were adopted[7]. The compositions of the simulated electrolytes were given in Table S4. Parameter fitting was performed using the density functional theory (DFT) package Gaussian16[8] under B3LYP exchange-correlation functional with Grimme's DFT-D3(BJ) empirical dispersion correction,[9] and the def2-TZVP (for SCN) and the ma-TZVP (for FSI^-) basis set was adopted for self-consistent field (SCF) calculations. The RESP2 (0.5)[10] charges combining gas- and liquid-phase (H_2O or H_2O/SCN implicit solvent, PCM model) charges were adopted for FSI^- anions and SCN molecules in this work calculated using Gaussian16 and Multiwfn package.[11] The initial structures were modeled via Packmol package[12] and the Moltemplate package.[13] The systems were then subjected to a simulated annealing equilibration protocol as follows: (1) equilibration at T = 298 K for 2 ns in the NPT ensemble; (2) heating up the system to 500 K over 2 ns in NPT ensemble; (3) relaxation at T = 500 K over 2 ns in NPT ensemble; (4) cooling down to T = 298 K over 2 ns in NPT ensemble; (5) equilibration at T = 298 K for 50 ns in NPT ensemble. The production run was subsequently performed at T = 298 K over 50 ns in the NVT ensemble. All the simulations in this work used a timestep of 2 fs, and a pressure of 1 atm. The temperature and pressure were regulated with a Nose-Hoover thermostat and barostat, with a damping parameter of 0.2 ps and 2 ps respectively.

DFT calculations. The *ab initio* molecule dynamic (AIMD) simulations theoretically investigated the solution structure, as implemented in the computational software Vienna ab initio simulation package (VASP).[14] The projector augmented wave method was used for electronic structure calculation.[15] The exchange-correlation interaction was described by PBE functional with D4 dispersion correction from Grimme.[16] The cutoff energy and electronic energy self-consistency tolerance were set to 520 eV and 10^{-6} eV, respectively. The number ratios of K: H_2O: SCN for 30 m KFSI–H_2O and 5.6 m KFSI–SCN–H_2O solutions were 16:30:0 and 10:20:10, respectively. The gamma-point sampling was used for MD, and a $3 \times 3 \times 3$ k-point grid was used for density of states (DOS) calculations. The temperature of NVT ensemble was controlled using the Nose'-Hoover themostat. The solution was first equilibrated at a higher temperature (698 K, 5 ps) to generate configurations with fully mixed solvents and solutes. The high-temperature equilibrated solution structures are then used as the initial configurations for MD simulations at room temperature (298 K) for 5 ps before DOS calculations. The timestep for AIMD simulations was 2 fs.
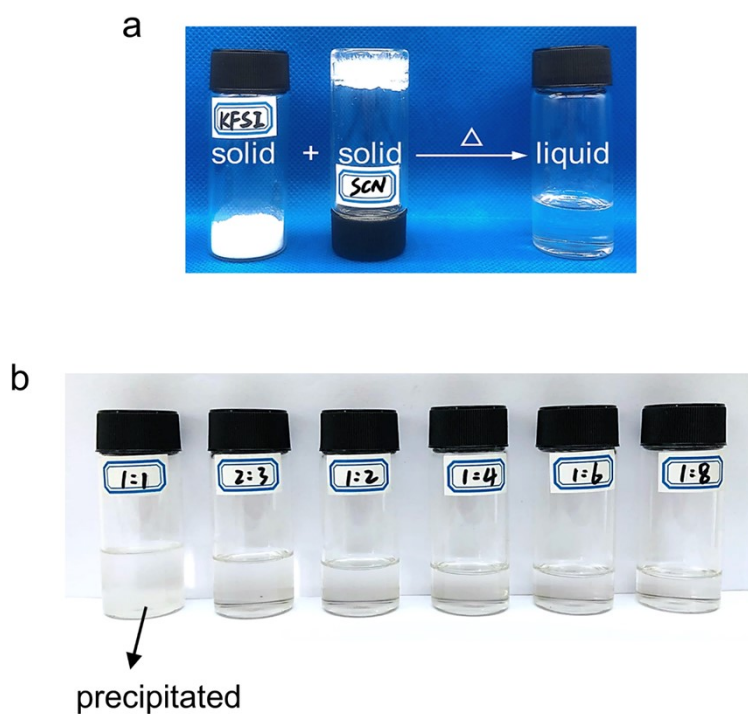
Figure S1. a) Preparation of KFSI/SCN eutectic electrolyte (liquid state can be obtained by heating a mixture of solid KFSI and solid SCN). b) Optical photographs of KFSI/SCN eutectic solutions at different molar ratios after standing for 72 h.
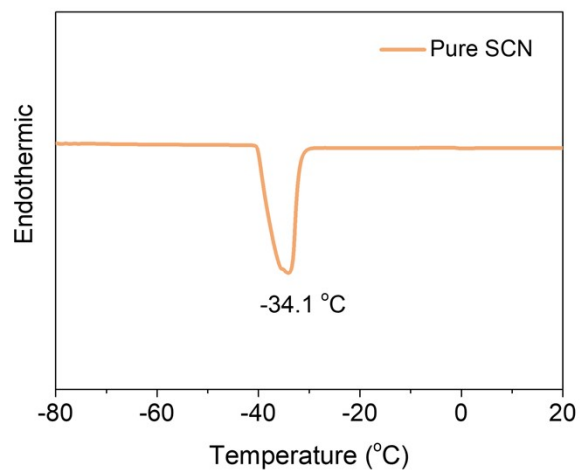
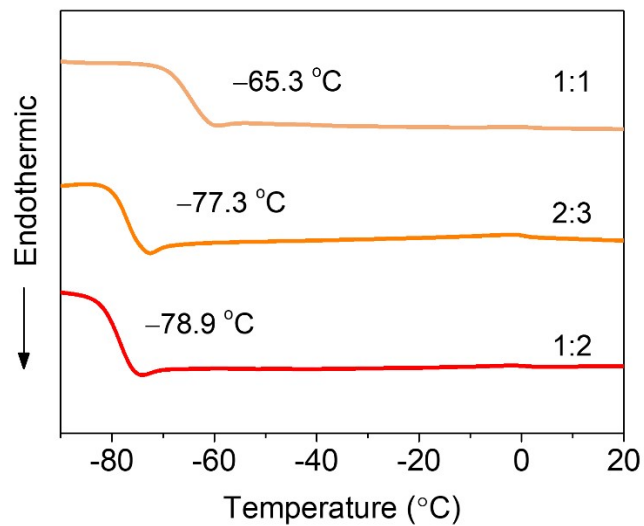**Figure S2.** The DSC result of pure SCN from −80°C to 20°C under N_2 atmosphere.

Figure S3. The DSC data of KFSI/SCN eutectic solutions at different molar ratios (1:1, 2:3, and 1:2).
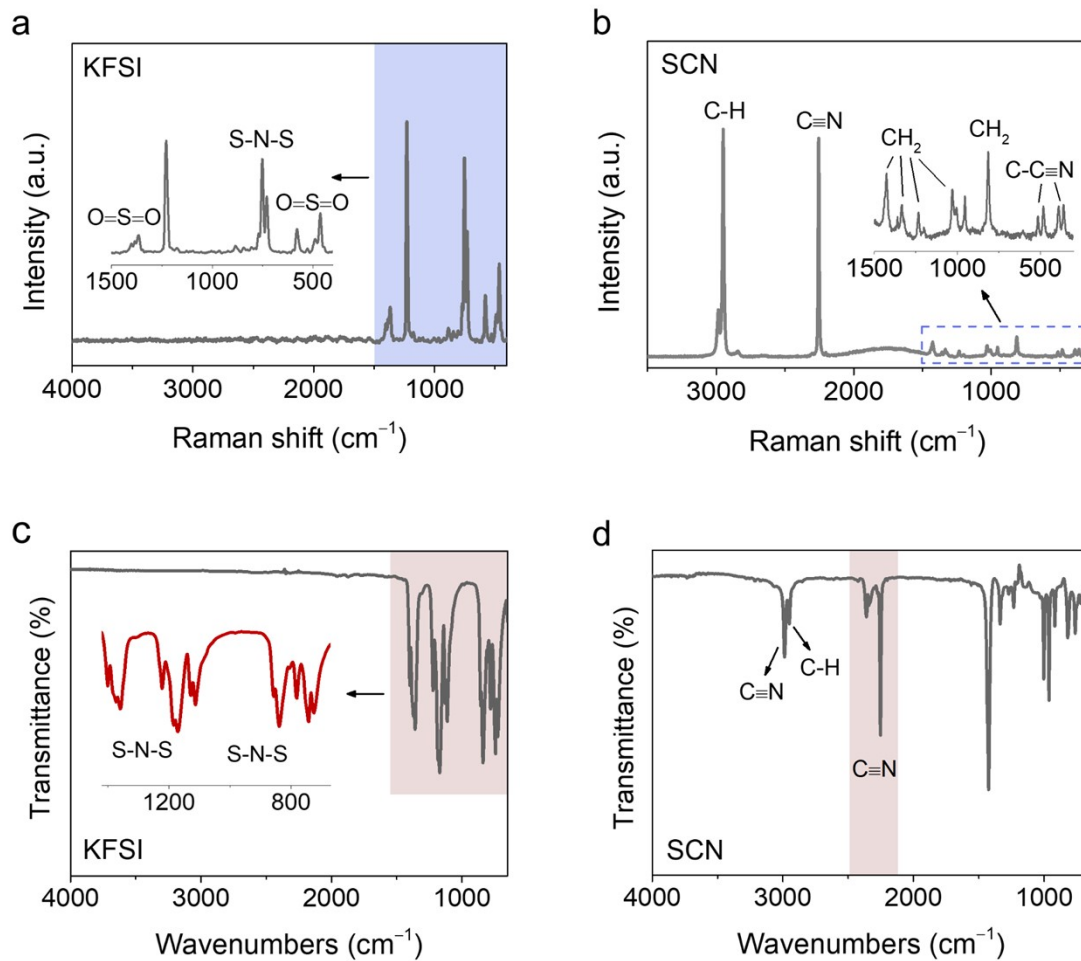
Figure S4. a), b) Raman spectra of solid KFSI and pure SCN. c), d) FTIR spectra of solid KFSI and pure SCN.
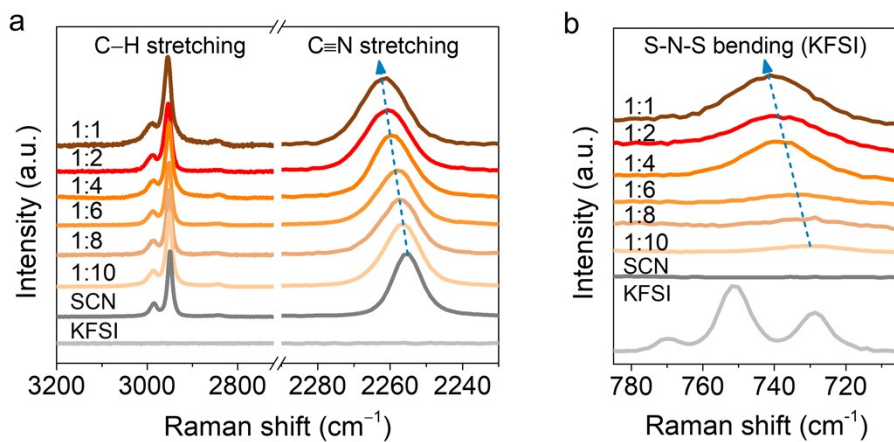
Figure S5. Raman spectra of KFSI/SCN systems at different KFSI concentrations. a) Progression of C≡N stretching vibration with increasing salt concentration. b) Progression of S−N−S bending vibration with increasing salt concentration.
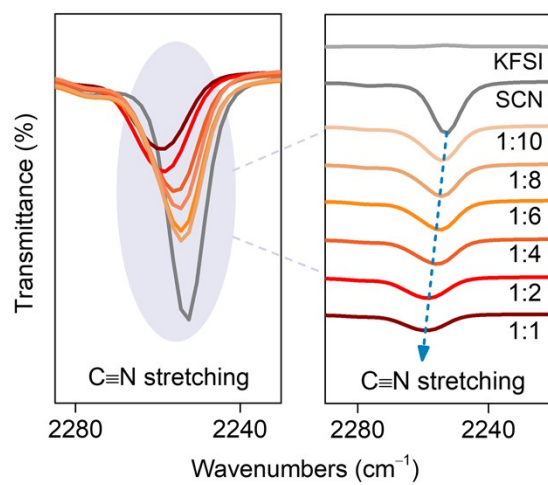
Figure S6. The ATR–FTIR spectra of KFSI/SCN eutectic solutions at different molar ratios.
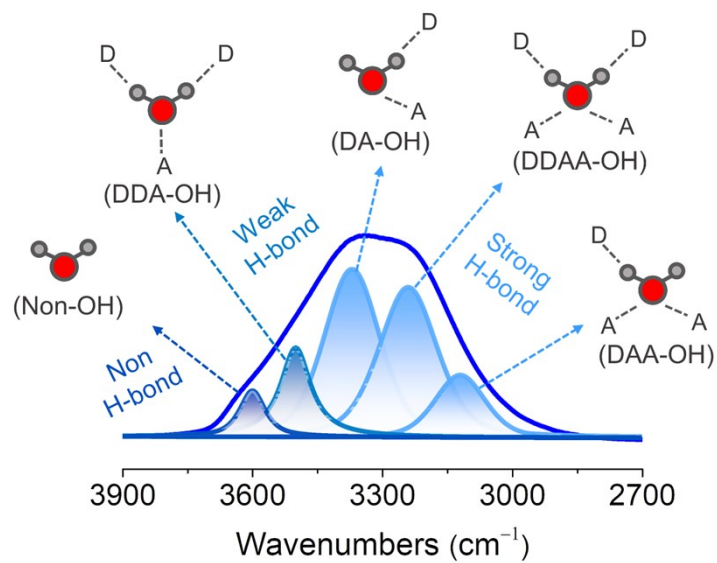
Figure S7. Schematic illustration representing the O–H stretching of pure H_2O (including DAA–OH, DDAA–OH, DA–OH, DDA–OH, and Non–OH, where D means donor and A means acceptor).
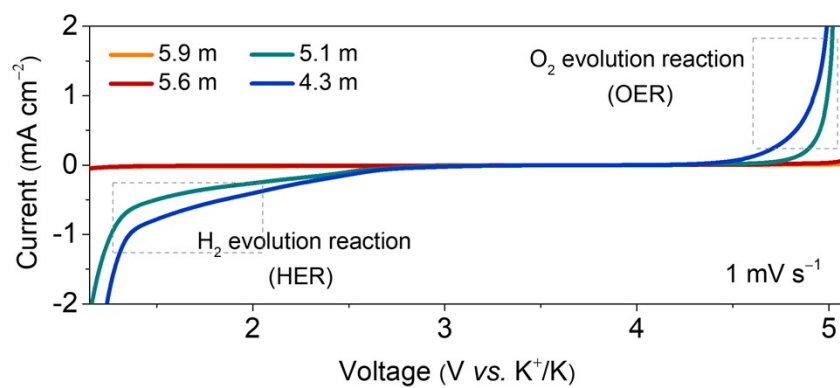
Figure S8. The LSV results of different KFSI–SCN–H_2O hybrid electrolytes at 1 mV s^{-1}.
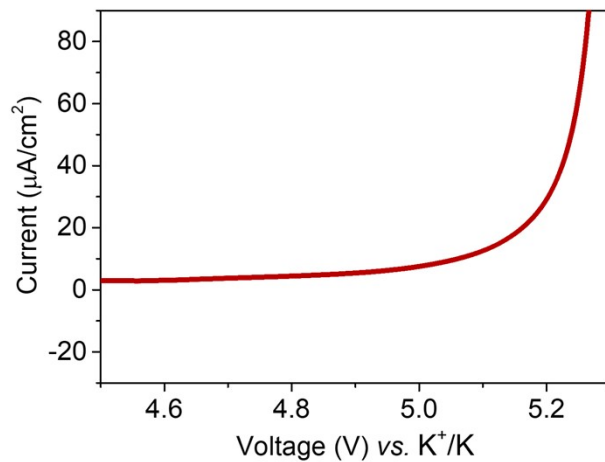
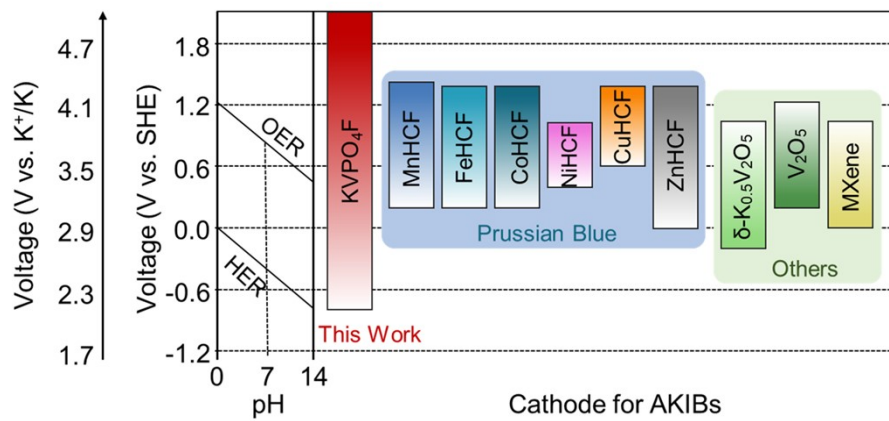**Figure S9.** The enlarged LSV curve with a smaller current range more clearly reflects the high anodic limit.

Figure S10. Comparison of the operating voltage window of KVPO₄F with other commonly used cathode materials in AKIBs.
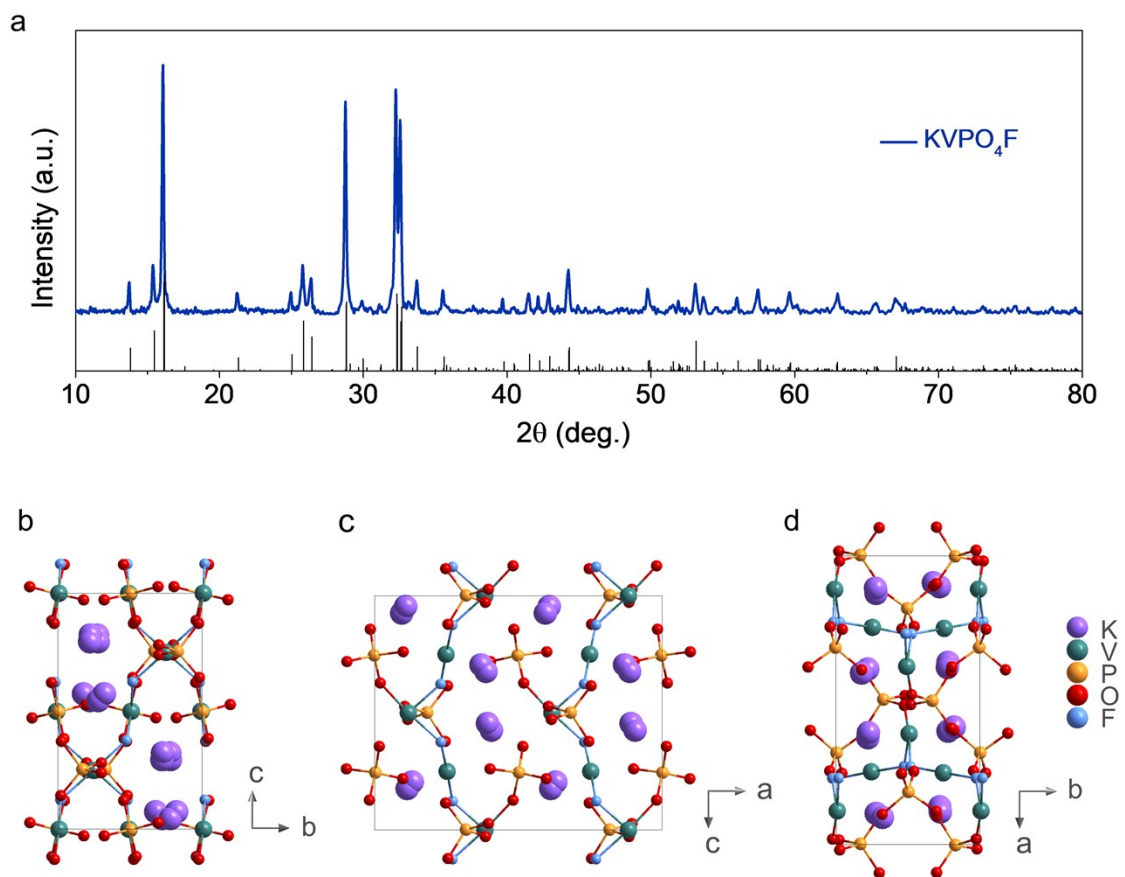
Figure S11. a) The XRD pattern of the synthesized KVPO$_4$F material. b–d) The structures of the KVPO$_4$F material along *a*, *b*, and *c* axes, respectively.
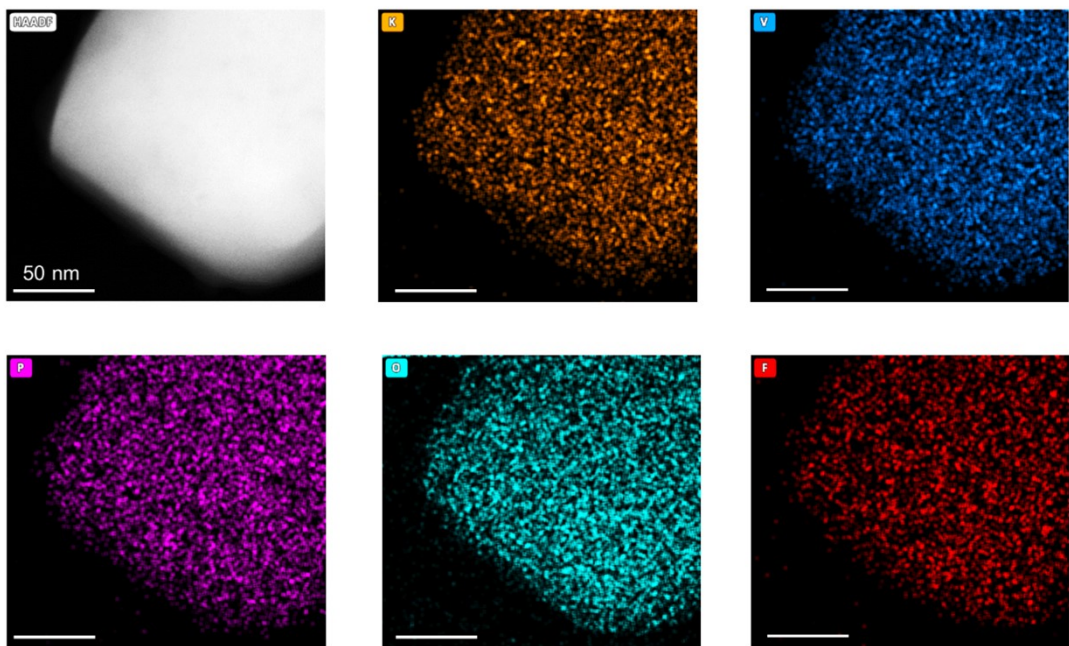
Figure S12. HAADF–STEM EDS mapping of the synthesized KVPO$_4$F material (K: orange, V: blue, P: purple, O: green, F: red).
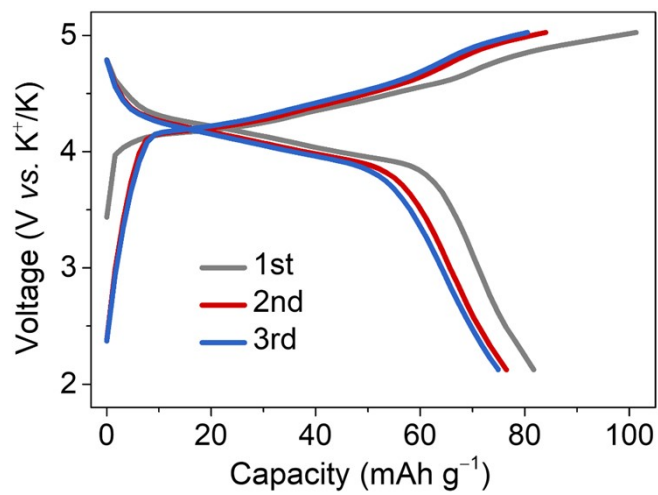
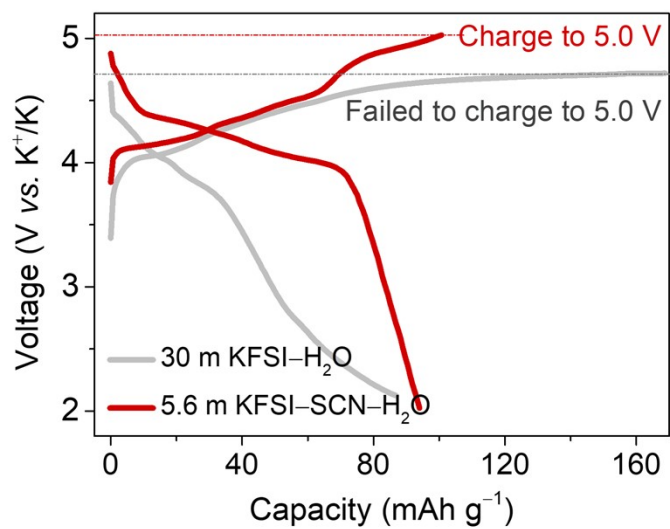**Figure S13.** The first three charge–discharge profiles of $KVPO_4F$ cathode in the 5.6 m KFSI–SCN–H_2O electrolyte.

Figure S14. Comparison of typical charge–discharge profiles of the $KVPO_4F$ cathode in 30 m $KFSI–H_2O$ and 5.6 m $KFSI–SCN–H_2O$ electrolytes.
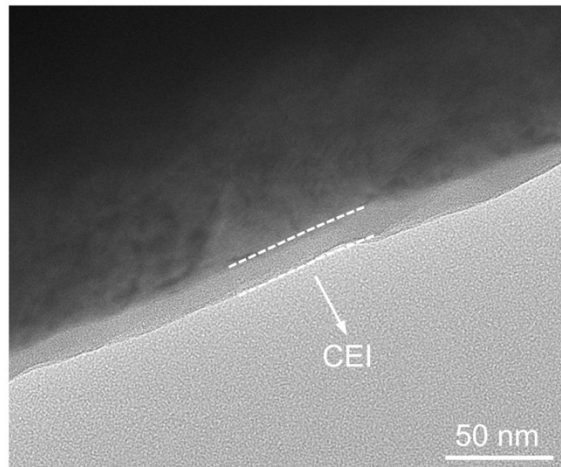
Figure S15. TEM morphology of the CEI on the surface of the cycled KVPO$_4$F cathode.
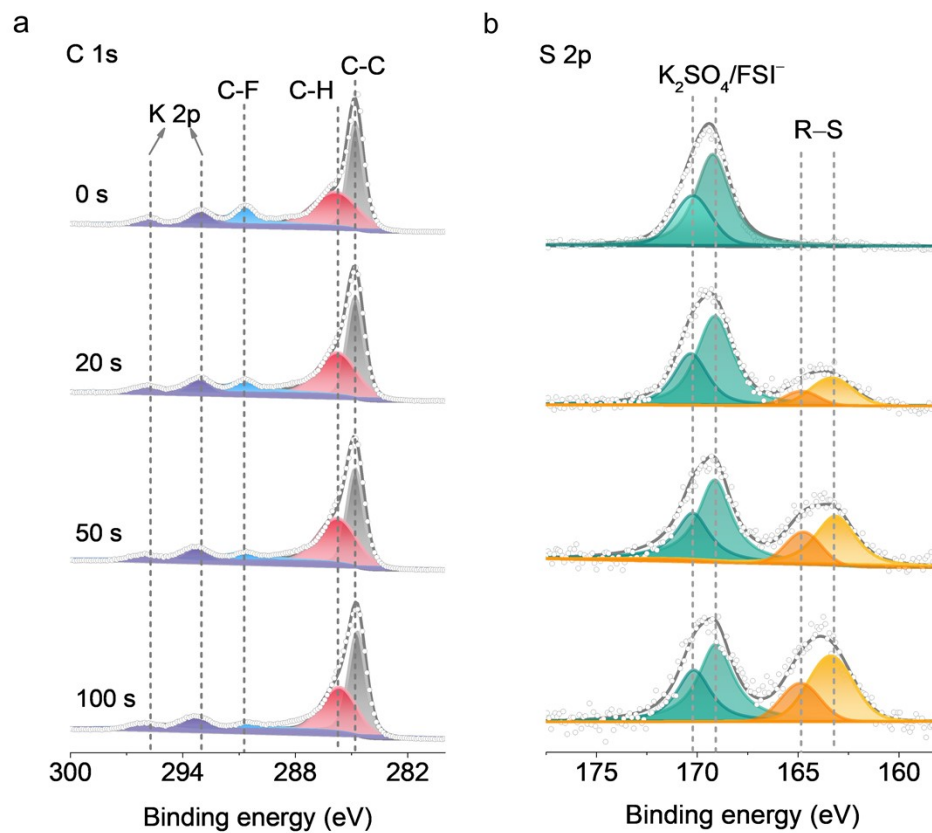
Figure S16. XPS depth profiles of the cycled $KVPO_4F$ electrode upon Ar^+ sputtering for C 1s (a) and S 2p (b).
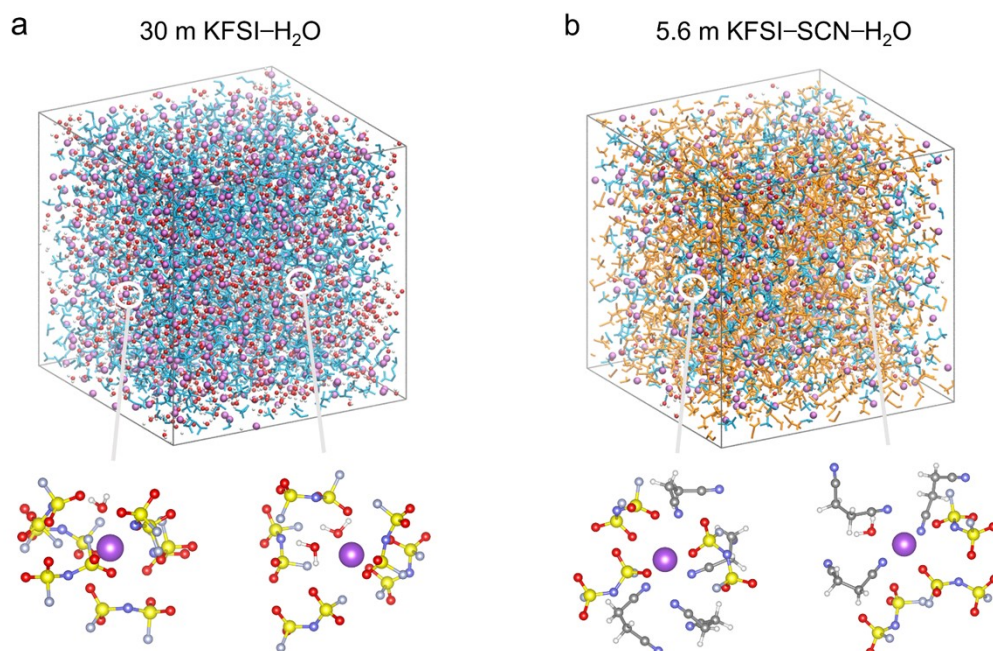
Figure S17. a) The typical local coordination among K^+, FSI^-, and H_2O in 30 m KFSI–H_2O electrolyte. b) The typical local coordination among K^+, FSI^-, H_2O, and SCN in 5.6 m KFSI–SCN–H_2O electrolyte. [K^+ (purple), FSI^- (blue), SCN (orange), and H_2O (red, white)].
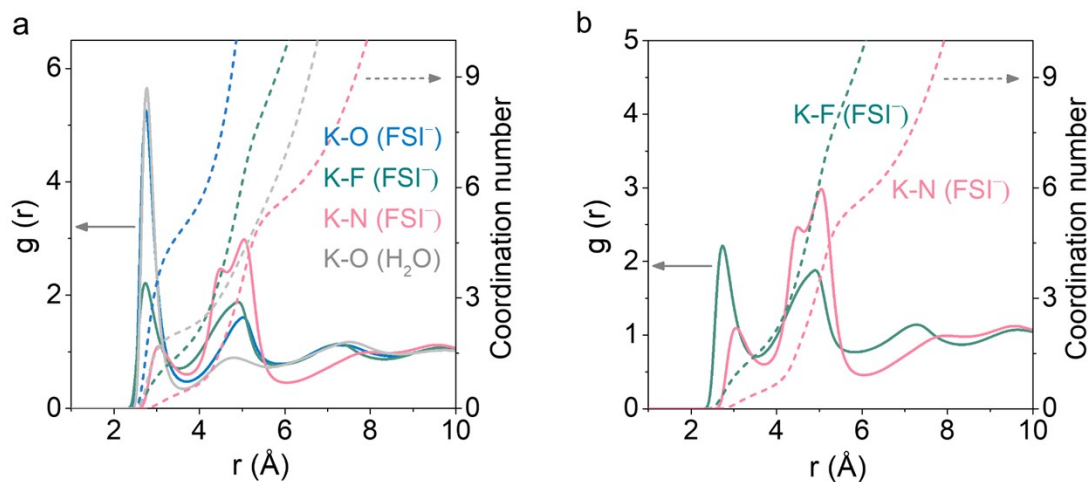
Figure S18. a) RDF plots and coordination numbers (K^+ as the center) in the 30 m KFSI–H_2O electrolyte. b) An enlarged view of K−F (FSI⁻) and K−N (FSI⁻). [The solid curves represent g (r), and the dashed curves are their integral results, representing the coordination numbers].

Figure S19. a) RDF plots and coordination numbers (K^+ as the center) in the 5.6 m KFSI–SCN–H_2O hybrid electrolyte. b) An enlarged view of K−F (FSI^-) and K−N (FSI^-). [The solid curves represent g (r), and the dashed curves are their integral results, representing the coordination numbers].
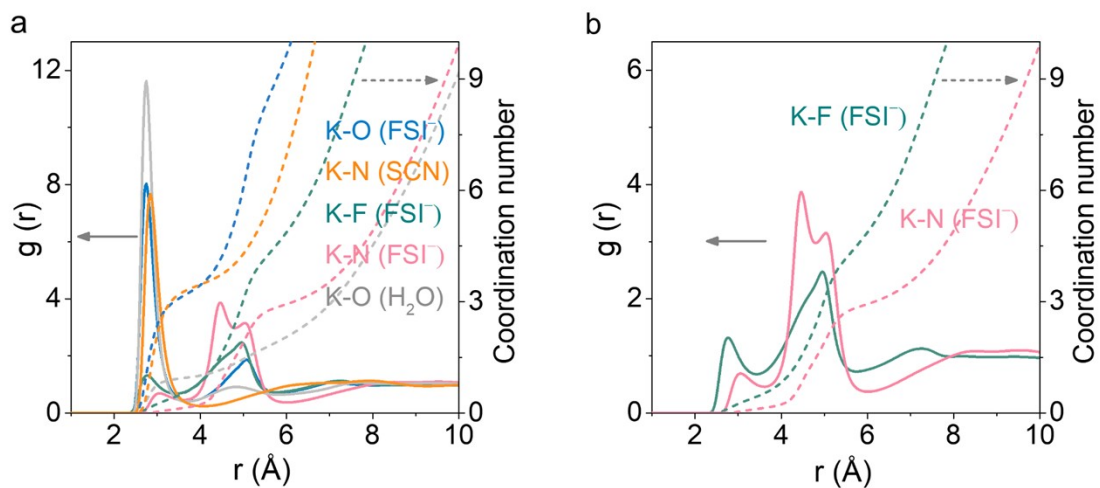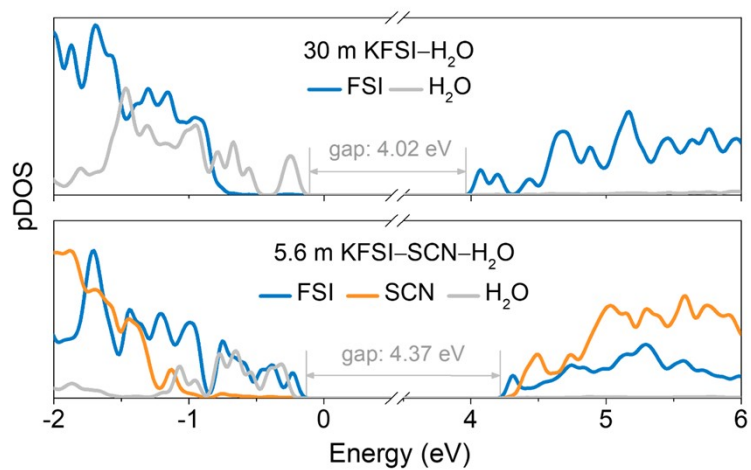
Figure S20. The calculated pDOS of the 30 m KFSI–H_2O electrolyte (top) and the 5.6 m KFSI–SCN–H_2O (bottom) hybrid electrolytes.
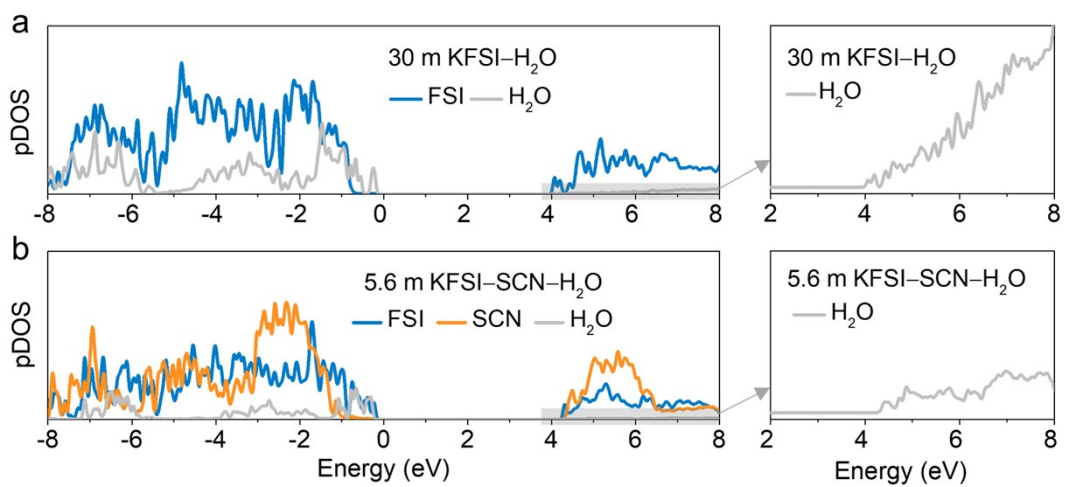
Figure S21. The enlarged view of H_2O molecular orbitals in the calculated pDOS of the 30 m KFSI–H_2O electrolyte (a) and the 5.6 m KFSI–SCN–H_2O (b) hybrid electrolyte.
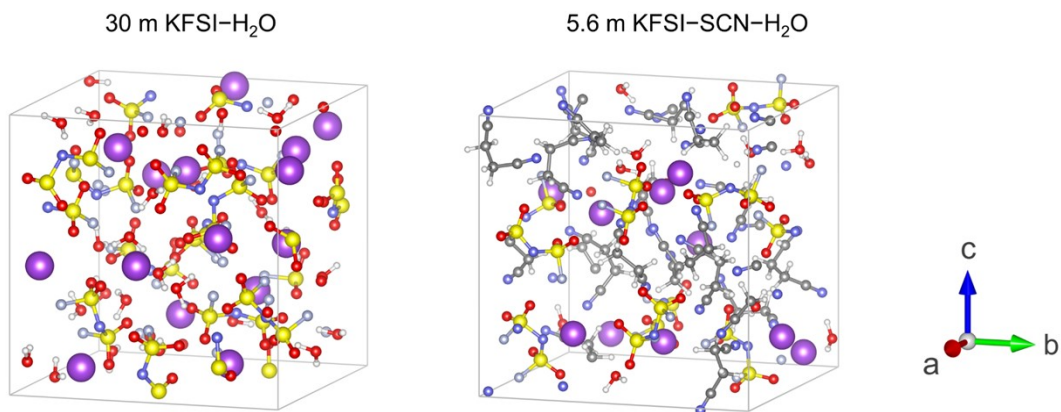
Figure S22. The *ab initio* MD simulation boxes of the 30 m KFSI–H_2O electrolyte (left) and the 5.6 m KFSI–SCN–H_2O (right) hybrid electrolyte for pDOS calculations.

the highest occupied molecular orbital   the lowest unoccupied molecular orbital
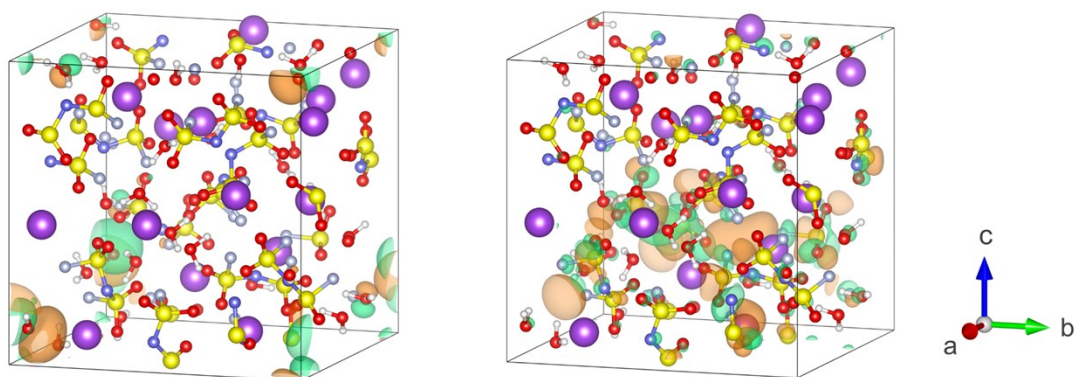
Figure S23. The highest occupied molecular orbital (left) and the lowest unoccupied molecular orbital (right) in the simulated solvation structures of 30 m KFSI–H_2O electrolyte.
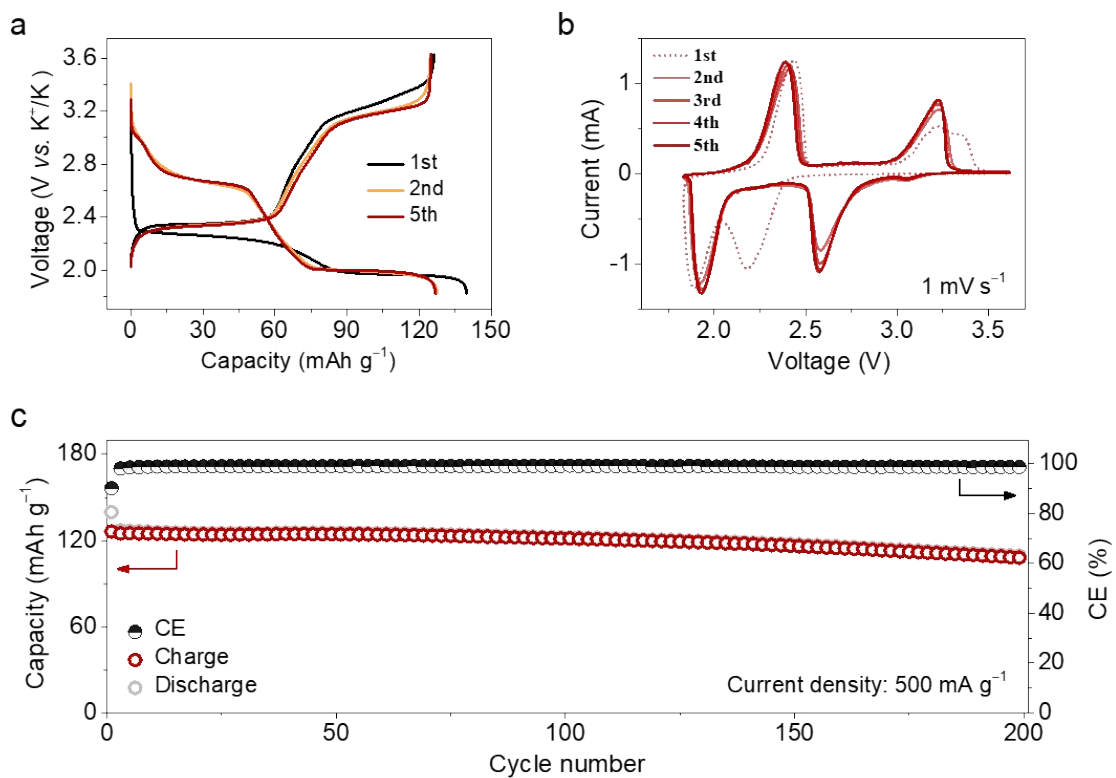
Figure S24. The electrochemical performance of PTCDI anode in the 5.6 m KFSI–SCN–H$_2$O electrolyte. a) Charge–discharge profiles. b) Cyclic voltammetry curves. c) long-term cycling stability and corresponding CE at 500 mA g^{-1}.
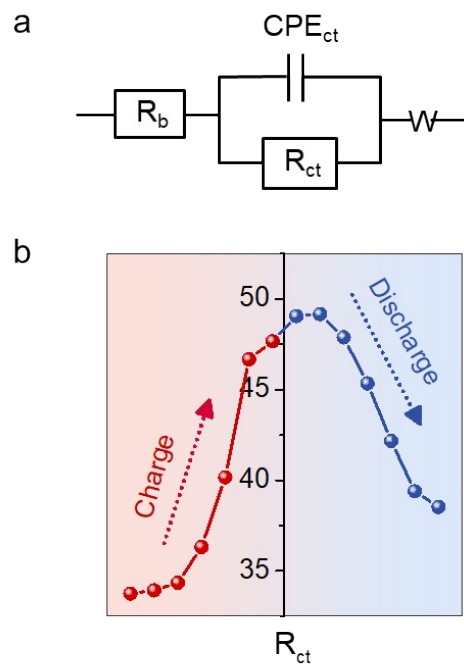
Figure S25. a) The fitting equivalent circuit used for *in situ* EIS analysis. (b) The variation of the R_{ct} value of the KVPO$_4$F‖PTCDI full cell during the first cycle.
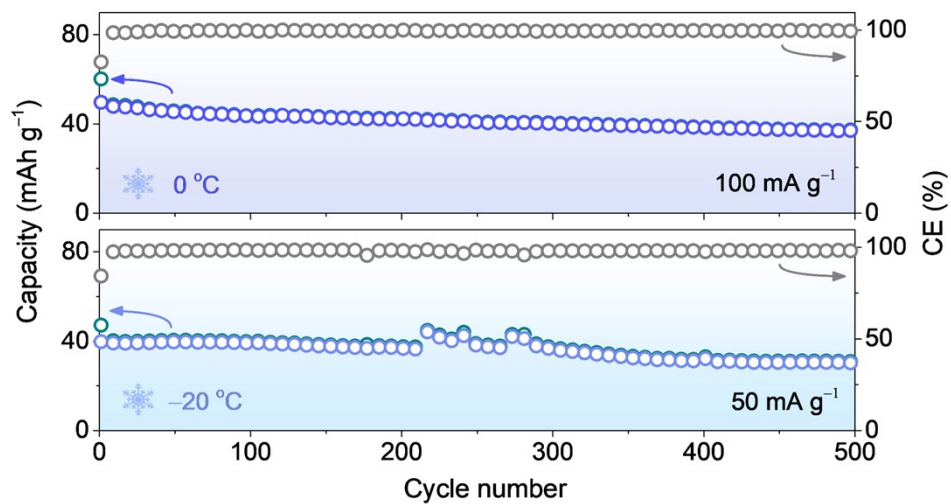
Figure S26. The electrochemical performance of KVPO$_4$F‖PTCDI full cell at low temperatures (0 °C and −20 °C).
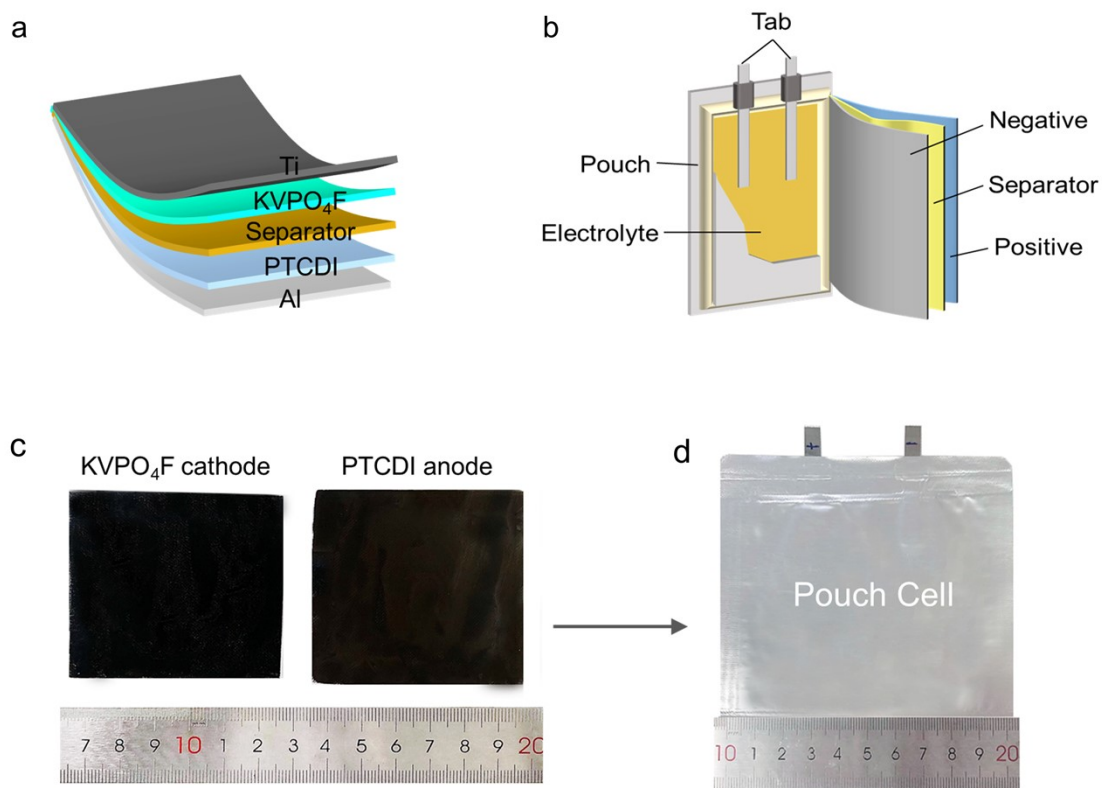
Figure S27. Preparation of pouch cell. a), b) Schematic diagram of the hierarchical structure of electrodes and the pouch cell. c), d) Optical photographs of the prepared KVPO$_4$F cathode and PTCDI anode with a large area and the assembled aqueous K-ion pouch cell with the 5.6 m KFSI–SCN–H$_2$O electrolyte.

Table S1. Compositions of different KFSI–SCN–H$_2$O hybrid electrolytes.

Sample	Salt (molarity, mol kg^{-1})	Solvent (molar ratio)
5.9 m KFSI–SCN–H$_2$O	5.9 m KFSI	SN:H$_2$O (4:1)
5.6 m KFSI–SCN–H$_2$O	5.6 m KFSI	SN:H$_2$O (2:1)
5.1 m KFSI–SCN–H$_2$O	5.1 m KFSI	SN:H$_2$O (1:1)
4.3 m KFSI–SCN–H$_2$O	4.3 m KFSI	SN:H$_2$O (1:2)
3.2 m KFSI–SCN–H$_2$O	3.2 m KFSI	SN:H$_2$O (1:4)

Table S2. Comparison of electrochemical stability window of the 5.6 m KFSI–SCN–H$_2$O with other reported aqueous K-ion electrolytes.

Electrolytes	Cathodic potential (V)	Anodic potential (V)	References
Pure H$_2$O	2.53	3.76	/
Saturated KNO$_3$	2.07	4.27	*J. Energy Chem.* **48**, 14–20 (2020)[17]
22 M KCF$_3$SO$_3$	1.83	4.83	*Nat. Energy* **4**, 495–503 (2019)[18]
40 M HCOOK	0.63	4.63	*Chem. Commun.* **55**, 12817–12820 (2019)[19]
30 m KAc	1.43	4.63	*ACS Energy Lett.* **3**, 373–374 (2018)[20]
16 m KF	1.83	5.23	*Nano Energy* **99**, 107377 (2022)[21]
K–H$_2$O$_{2.8}$–TMP$_{4.9}$	1.28	4.68	*Adv. Funct. Mater.* **33**, 2215027 (2023)[22]
2 m KFSI–DMF–H$_2$O	1.88	4.77	*ACS Appl. Mater. Interfaces* **13**, 38248–38255 (2021)[23]
5.6 m KFSI–SCN–H$_2$O	1.13	**5.13**	**This work**

The potential has been converted to K$^+$/K reference for convenience.
m: mol kg^{-1}, M: mol L^{-1}

Table S3. Comparison of electrochemical performance of $KVPO_4F$ in this work with other reported cathode materials in aqueous K-ion batteries.

Materials	Upper voltage (V)	Discharge capacity (mAh g^{-1})	Capacity retention (%)	Discharge plateau (V)	Cycle number
$K_{1.85}Fe_{0.33}Mn_{0.67}[Fe(CN)_6]_{0.98}\cdot0.77H_2O$ (MnHCF)[18]	4.3	94	90	3.9	10000
$Fe_4[Fe(CN)_6]_3\cdot3.4H_2O$ (FeHCF)[24]	4	62	80.8	3.4	1000
$K_{1.43}Co[Fe(CN)_6]_{0.94}\cdot1.87H_2O$ (CoHCF)[25]	4.3	76.8	70	3.7	1000
$K_{0.6}Ni_{1.2}Fe(CN)_6\cdot3.6H_2O$ (NiHCF)[26]	3.9	51.3	93	3.6	5000
$K_{0.71}Cu[Fe(CN)_6]_{0.72}\cdot3.7H_2O$ (CuHCF)[27]	4.3	52.2	83	3.9	>10000
Mxene[28]	3.9	56.4	89.7	3.3	>10000
$KVPO_4F$ (this work)	**5**	**80**	**80.3**	**4**	**10000**

The corresponding abbreviations of cathode materials are written in parentheses.

Table S4. MD simulations of 30 m KFSI–H_2O and 5.6 m KFSI–SCN–H_2O electrolytes.

	30 m KFSI (KFSI:H_2O=1:1.8, molar ratio)	5.6 m KFSI–SCN–H_2O (KFSI:SCN:H_2O=1:2:1, molar ratio)
Number of KFSI per box	800	380
Number of H_2O per box	1480	365
Number of SCN per box	/	760
Total number of atoms	12440	12495
Simulation box size ($Å^3$)	163468.75	167241.42
MD, density (g cm^{-3})	2.053	1.497
Bias temperature (K)	298	298

Table S5. Comparison of the energy density in the reported aqueous K-ion full cells.

Full cell configuration[a]	Energy density[b] (Wh kg^{-1})	References
$K_{1.85}Fe_{0.33}Mn_{0.67}[Fe(CN)_6]_{0.98}\cdot 0.77H_2O$‖PTCDI (KFeMnHCF-3565‖PTCDI)	80	*Nat. Energy* **4**, 495–503 (2019)[18]
$K_{1.82}Mn[Fe(CN)_6]_{0.96}\cdot 0.47H_2O$‖PTCDI (KMnHCF‖PTCDI)	92	*Nat. Sustainability* **5**, 225–234 (2021)[29]
$K_2Zn_3[Fe(CN)_6]_2$‖$KTi_2(PO_4)_3$ (KZnHCF‖KTP)	53	*ACS Appl. Mater. Interfaces* **13**, 38248–38255 (2021)[23]
$K_2FeFe(CN)_6$‖$KTi_2(PO_4)_3$ (KFeHCF‖KTP)	47	*J. Mater. Chem. A* **9**, 2822–2829 (2021)[30]
$FeFe(CN)_6$‖PNTCDA (FeHCF‖PNTCDA)	47	*J. Energy Chem.* **48**, 14–20 (2020)[17]
$K_2NiFe(CN)_6\cdot 1.2H_2O$‖$NaTi_2(PO_4)_3$ (KNiHCF‖NTP)	64	*Adv. Energy Mater.* **8**, 1801413 (2018)[31]
$KVPO_4F$‖PTCDI	**100**	**This work**

[a] The corresponding abbreviations of full cell configuration are written in parentheses.

[b] The energy density of the full cell was calculated based on the equation below:

Energy density = capacity × average voltage / total mass of both electrodes

PTCDI: 3,4,9,10-perylenetetracarboxylic diimide.

PNTCDA: 1,4,5,8-naphthalenetetracarboxylic dianhydride-derived polyimide.

Other supplementary materials for this manuscript include the following:

Movie S1 (separate file). Flammability test of KFSI/SCN eutectic solution.

Movie S2 (separate file). Flammability test of 5.6 m KFSI–SCN–H$_2$O hybrid electrolyte.

References

1. J. Yu, C. Yu, W. Guo, Z. Wang, Y. Ding, Y. Xie, K. Liu, H. Wang, X. Tan, H. Huang and J. Qiu, *Adv. Funct. Mater.*, 2022, **32**, 2204609.
2. A. P. Thompson, H. M. Aktulga, R. Berger, D. S. Bolintineanu, W. M. Brown, P. S. Crozier, P. J. in 't Veld, A. Kohlmeyer, S. G. Moore, T. D. Nguyen, R. Shan, M. J. Stevens, J. Tranchida, C. Trott and S. J. Plimpton, *Comput. Phys. Commun.*, 2022, **271**, 108171.
3. G. A. Kaminski, R. A. Friesner, J. Tirado-Rives and W. L. Jorgensen, *J. Phys. Chem. B*, 2001, **105**, 6474-6487.
4. J. N. Canongia Lopes, K. Shimizu, A. A. H. Pádua, Y. Umebayashi, S. Fukuda, K. Fujii and S. Ishiguro, *J. Phys. Chem. B*, 2008, **112**, 9449-9455.
5. L. S. Dodda, I. Cabeza de Vaca, J. Tirado-Rives and W. L. Jorgensen, *Nucleic Acids Res.*, 2017, **45**, W331-W336.
6. L. P. Wang, T. J. Martinez and V. S. Pande, *J. Phys. Chem. Lett.*, 2014, **5**, 1885-1891.
7. A. Sengupta, Z. Li, L. F. Song, P. Li and K. M. Merz, Jr., *J. Chem. Inf. Model.*, 2021, **61**, 869-880.
8. M. J. Frisch, G. W. Trucks, H. B. Schlegel, G. E. Scuseria, M. A. Robb, J. R. Cheeseman, G. Scalmani, V. Barone and G. A. Petersson, *Gaussian 16*, Revision B.01, 2016.
9. S. Grimme, J. Antony, S. Ehrlich and H. Krieg, *J. Chem. Phys.*, 2010, **132**, 154104.
10. M. Schauperl, P. S. Nerenberg, H. Jang, L. P. Wang, C. I. Bayly, D. L. Mobley and M. K. Gilson, *Commun. Chem.*, 2020, **3**, 44.
11. T. Lu and F. Chen, *J. Comput. Chem.*, 2012, **33**, 580-592.
12. L. Martinez, R. Andrade, E. G. Birgin and J. M. Martinez, *J. Comput. Chem.*, 2009, **30**, 2157-2164.
13. A. I. Jewett, D. Stelter, J. Lambert, S. M. Saladi, O. M. Roscioni, M. Ricci, L. Autin, M. Maritan, S. M. Bashusqeh, T. Keyes, R. T. Dame, J. E. Shea, G. J. Jensen and D. S. Goodsell, *J. Mol. Biol.*, 2021, **433**, 166841.
14. G. Kresse and J. Furthmüller, *Comput. Mater. Sci.*, 1996, **6**, 15-50.
15. J. P. Perdew, K. Burke and M. Ernzerhof, *Phys. Rev. Lett.*, 1996, **77**, 3865-3868.
16. E. Caldeweyher, C. Bannwarth and S. Grimme, *J. Chem. Phys.*, 2017, **147**, 034112.
17. M. Wang, H. Wang, H. Zhang and X. Li, *J. Energy Chem.*, 2020, **48**, 14-20.
18. L. Jiang, Y. Lu, C. Zhao, L. Liu, J. Zhang, Q. Zhang, X. Shen, J. Zhao, X. Yu, H. Li, X. Huang, L. Chen and Y.-S. Hu, *Nat. Energy*, 2019, **4**, 495-503.
19. T. Liu, L. Tang, H. Luo, S. Cheng and M. Liu, *Chem. Commun.* , 2019, **55**, 12817-12820.
20. D. P. Leonard, Z. Wei, G. Chen, F. Du and X. Ji, *ACS Energy Lett.*, 2018, **3**, 373-374.
21. R. Hou, Y. Wang, Y. Sun, J. Lang, S. Yang and X. Yan, *Nano Energy*, 2022, **99**, 107377.
22. J. Chen, S. Lei, S. Zhang, C. Zhu, Q. Liu, C. Wang, Z. Zhang, S. Wang, Y. Shi, L. Yin and R. Wang, *Adv. Funct. Mater.*, 2023, **33**, 2215027.
23. X. Yuan, Y. Li, Y. Zhu, W. Deng, C. Li, Z. Zhou, J. Hu, M. Zhang, H. Chen and R. Li, *ACS Appl. Mater. Interfaces*, 2021, **13**, 38248-38255.
24. M. Xia, X. Zhang, T. Liu, H. Yu, S. Chen, N. Peng, R. Zheng, J. Zhang and J. Shu, *Chem. Eng. J.*, 2020, **394**, 124923.
25. K. Zhu, Z. Li, T. Jin and L. Jiao, *J. Mater. Chem. A*, 2020, **8**, 21103-21109.

26. C. D. Wessells, S. V. Peddada, R. A. Huggins and Y. Cui, *Nano Lett.*, 2011, **11**, 5421-5425.
27. C. D. Wessells, R. A. Huggins and Y. Cui, *Nat. Commun.*, 2011, **2**, 550.
28. G. Liang, X. Li, Y. Wang, S. Yang, Z. Huang, Q. Yang, D. Wang, B. Dong, M. Zhu and C. Zhi, *Nano Research Energy*, 2022, **1**, e9120002.
29. J. Ge, L. Fan, A. M. Rao, J. Zhou and B. Lu, *Nat. Sustain.*, 2021, **5**, 225-234.
30. Y. Li, W. Deng, Z. Zhou, C. Li, M. Zhang, X. Yuan, J. Hu, H. Chen and R. Li, *J. Mater. Chem. A*, 2021, **9**, 2822-2829.
31. W. Ren, X. Chen and C. Zhao, *Adv. Energy Mater.*, 2018, **8**, 1801413.